Comparison of TE and TM Inversions in the Framework of the Gauss-Newton Method

Puyan Mojabi, *Student Member, IEEE*, and Joe LoVetri, *Senior Member, IEEE*

***Abstract*—The Gauss-Newton inversion method in conjunction with a regularized formulation of the inverse scattering problem is used to invert transverse electric (TE) and transverse magnetic (TM) data. The utilized data sets consist of experimental data provided by the Institut Fresnel as well as synthetic data. The TE inversion outperformed the TM inversion when utilizing near-field scattering data collected using only a few transmitters and receivers. However, very little difference was found between TE and TM inversions when using far-field scattering data. It is conjectured that the reason for the better performance of the near-field TE result is that the near-field TE data contains more information than the near-field TM data at each receiver point. In all cases considered herein, the TE inversion required equal or fewer iterations than the TM inversion. The per-iteration computational complexity of both TE and TM inversions is discussed in the framework of the Gauss-Newton inversion method. Actual costs are consistent with the computational complexity analysis that is given.**

***Index Terms*—Gauss-Newton method, inverse problems, microwave imaging, remote sensing.**

I. Introduction

THE electromagnetic inverse scattering problem considered herein consists of determining the electric constitutive parameters, i.e., permittivity and conductivity, of an unknown object inside a bounded imaging domain located in a known background medium. The inversion is obtained from measured field data exterior to the imaging domain when it is irradiated by a number of known incident fields. It is well-known that the inverse scattering problem is ill-posed: the solution to the mathematical problem is not guaranteed to be unique for most measurement configurations and does not depend continuously on the measured data [1]. This ill-posedness is usually treated by employing different regularization techniques.

The other difficulty in solving the inverse scattering problem is that it is nonlinear with respect to the unknown contrast. The nonlinearity of the problem has led to the development of various iterative techniques during the past two decades. These iterative techniques attempt to minimize an appropriately constructed cost-functional. Two approaches based on the formulation of the problem using two different cost-functionals have been successfully used to solve the inverse scattering problem. The first approach, which includes the Gauss-Newton inversion (GNI) method, uses the conventional cost-functional which is based on the difference between the measured and predicted scattered data for a particular choice of the material parameters; see for example [2]–[13]. The conventional cost-functional is usually augmented by various regularization techniques. The second approach, which includes the modified gradient method (MGM) [14] and the Contrast Source Inversion (CSI) method [15], uses the same conventional cost-functional, formulated in terms of contrast sources, in the case of CSI, added to an error functional involving the domain integral equation which relates the fields inside the imaging domain to the constitutive parameters of the unknown object. This latter functional is formulated in terms of the contrast and contrast sources.

Although researchers have developed full-vectorial 3D inversion algorithms [5], [16], [17] (also see the papers in *Inverse Problems* special section [18]), the 2D algorithms considered herein are also very important because of their use in existing experimental systems. For example, in the microwave biomedical imaging systems developed at Dartmouth College for breast cancer imaging, the data is collected in seven different planes and a 2D Transverse magnetic (TM) GNI algorithm is used to invert the data [7]. The usefulness of this 2D assumption for biomedical imaging has been verified in [19]. Various 2D TM inversion algorithms have been tested with experimental data whereas only a few 2D Transverse Electric (TE) inversion methods have been investigated against experimental data. The 2D TM problem can be formulated as a scalar problem for a single electric field component. This is not the case for 2D TE problems where both electric field components in the transverse plane need to be taken into account in the formulation which results in a more complex (i.e., vectorial) formulation compared to the TM case. It should be noted that TE problems can also be formulated as scalar problems for a single magnetic field component. However, for the TE inversion, it has been shown in [20] that inverting the integral equation of the two electric field components is more stable and has better performance than inverting the integral equation of the single magnetic field component. From a physical perspective, the TE-polarized case includes polarization charges at dielectric discontinuities, which are difficult to model numerically [21]. On the other hand, TE-polarized data may contain more useful information about the object of interest as it is based on two different components of the electric field as opposed to one in the TM-polarized case. Note that these two polarizations are physically uncoupled: they provide independent information about the object being imaged. This fact can be used to improve the reconstruction in tomographic configurations by either simultaneously inverting TE and TM data [22] or using a cascaded TE-TM algorithm [23], [24].

Manuscript received March 14, 2009; revised August 24, 2009. Date of manuscript acceptance October 18, 2009; date of publication January 26, 2010; date of current version April 07, 2010. This work was supported by the Natural Sciences and Engineering Research Council (NSERC) of Canada, MITACS and CancerCare Manitoba.

The authors are with the Department of Electrical and Computer Engineering, University of Manitoba, Winnipeg, MB R3T5V6, Canada (e-mail: pmojabi@ee.umanitoba.ca).

Color versions of one or more of the figures in this paper are available online at http://ieeexplore.ieee.org.

Digital Object Identifier 10.1109/TAP.2010.2041156

There are only a few reports on the inversion of TE experimental data (using any method). In the special edition of *Inverse Problems* dedicated to inversions of the first Fresnel data set [25], only two papers dealt with the single TE case data that was provided: the first one [26] was concerned with determining the shape of the conducting u-shaped scatterer and the second one [27] used the multiplicative regularized contrast source inversion (MR-CSI) method to reconstruct the dielectric contrast of this scatterer. In the second special edition from *Inverse Problems* dedicated to the second Fresnel data set [28], [29], which includes TE and TM data for four targets, only two contributions addressed the TE-polarized data: the first one [30] applied the MR-CSI method to reconstruct the constitutive parameters of all the unknown objects in the data set and in the second contribution [31], a TM inversion algorithm based on the Diagonal Tensor Approximation and the Contrast Source Inversion method (DTA-CSI) was applied to invert the TE-polarized data. This last contribution uses a *calibration* of the TE data in a way that, according to the authors, allows the use of the scalar TM inversion algorithm. In addition, a 2D TE bi-conjugate gradient inversion method is used in [24] to reconstruct buried objects from experimental TE scattering data. In [32] an iterative multi-scaling approach was applied to the single u-shaped metal target case from the first Fresnel data set, in both TE and TM illuminations. Most recently, a TE stochastic inversion algorithm which utilizes a priori information about the object of interest has been used to reconstruct the second Fresnel data set [33].

In this paper, the GNI method is applied to a regularized formulation of the inverse scattering problem for inverting the complete second TE Fresnel data set which are combinations of lossless dielectric and metallic cylinders. As the Fresnel data contains only far-field scattering data, we also show the performance of the TE inversion against near-field synthetic scattering data. These TE inversions are compared with the TM inversions of the same targets. The motivation for moving to the near-field is that it is postulated that near-field TE data may contain more information than near-field TM data. This does not hold in the far-field, because in the far-field assuming $\boldsymbol{E} = E_\varphi \hat{\varphi}$, where $\boldsymbol{E}$ denotes the electric field and $\hat{\varphi}$ is shown in Fig. 1, is a good approximation for the TE case and E_φ is easily recoverable using measurements. In the near-field such an approximation is not valid and therefore two orthogonal field components need to be measured independently. This is difficult in practice and is one reason why 2D TE near-field microwave tomography systems have not been constructed in the past. It should be noted that the two orthogonal electric field components of TE near-field configurations can be extracted by measuring the single magnetic field component and then taking the derivative thereof. To compute an accurate derivative, magnetic field measurements must be performed in close proximities, which can cause difficulties in microwave tomography systems with co-resident antenna arrays (e.g., coupling between the co-resident antennas [34]). However, in TE far-field configurations, one can measure the single magnetic field component and then use a plane-wave approximation in order to extract the electric field from the magnetic field.

The result of the present investigation may be useful for justifying the added cost of developing such systems. The main contribution of this paper is to provide a quantitative comparison of TE and TM inversions of synthetic and experimental data sets for various cases including near-field and far-field imaging. This includes a comparison of computational complexity, image quality and convergence rate.

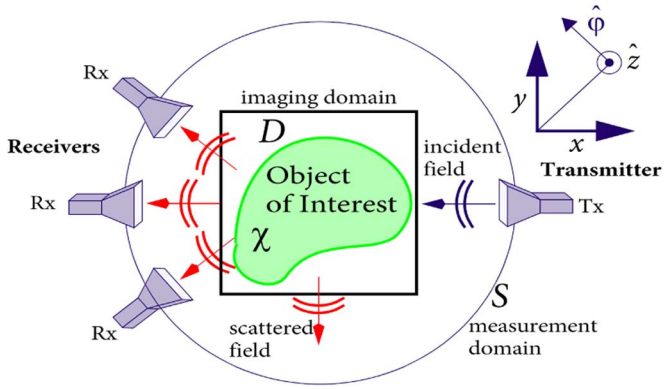

Fig. 1. Geometrical model of the inverse scattering problem ($\hat{z}$ is the unit vector pointing outside the x-y plane and $\hat{\varphi}$ is the unit vector in the azimuthal direction).

The paper is organized as follows. The formulation of the mathematical problem is given in Section II. Brief descriptions of the utilized Gauss-Newton inversion method and the forward solver used are given in Sections III and IV, respectively. A discussion of the computational complexity of the utilized algorithm for the TE and TM inversions is presented in Section V. Sections VI and VII provides the reconstruction results for all targets in the data sets. Finally, the results will be summarized in Section VIII.

II. Problem Statement

Consider a bounded imaging domain $\mathcal{D} \subset \mathbb{R}^2$ containing the object of interest and a measurement domain $\mathcal{S} \subset \mathbb{R}^2$ outside of $\mathcal{D}$ (see Fig. 1). Let $\boldsymbol{p}$ and $\boldsymbol{q}$ denote position vectors in the $x-y$ plane and define the complex electric contrast which is to be determined as

$$\chi(\boldsymbol{q}) = \frac{\epsilon(\boldsymbol{q}) - \epsilon_b}{\epsilon_b} \tag{1}$$

where ϵ_b is the background permittivity and $\epsilon(\boldsymbol{q})$ is the permittivity inside the imaging domain at the point $\boldsymbol{q}$. In general, these permittivities are complex to allow the modeling of lossy material. The total electric field is represented by two rectangular components, $\boldsymbol{E} = E_x\hat{x} + E_y\hat{y}$, in the TE case, and only one component, $\boldsymbol{E} = E_z\hat{z}$, in the TM case. The scattered electric field is then defined as $\boldsymbol{E}^{\text{scat}} = \boldsymbol{E} - \boldsymbol{E}^{\text{inc}}$ where $\boldsymbol{E}^{\text{inc}}$ denotes the incident field. Throughout the analysis, all material properties are taken to be non-magnetic: the permeability is taken as that of free-space, μ_0. The wavenumber of the background medium is denoted by $k_b = \sqrt{\omega^2\mu_0\epsilon_b}$. A time factor of $exp(-j\omega t)$ is implicitly assumed in this paper where $j^2 = -1$. The symbols ω and t represent the radial frequency and time respectively.

The so-called data equation in terms of the unknown contrast can be written as,

$$\boldsymbol{E}^{\mathrm{scat}}(\boldsymbol{p},\chi)=k_b^2\int_{\mathcal{D}}\bar{\bar{G}}(\boldsymbol{p},\boldsymbol{q})\cdot\chi(\boldsymbol{q})\boldsymbol{E}(\boldsymbol{q})d\boldsymbol{q} \tag{2}$$

where $\boldsymbol{p}\in\mathcal{S}$ and $\bar{\bar{G}}(\boldsymbol{p},\boldsymbol{q})$ is the dyadic Green's function for the background medium. Assuming the TE case, $\bar{\bar{G}}(\boldsymbol{p},\boldsymbol{q})$ may be written as [35],

$$\bar{\bar{G}}(\boldsymbol{p},\boldsymbol{q})=\left(\bar{\bar{I}}-\frac{1}{k_b^2}\nabla_{\boldsymbol{p}}\nabla_{\boldsymbol{q}}\right)G(\boldsymbol{p},\boldsymbol{q}). \tag{3}$$

Here $\bar{\bar{I}}$ is the 2D identity dyad and $G(\boldsymbol{p},\boldsymbol{q})$ is the 2D scalar Green's function for the homogeneous background. The symbol ∇ represents the gradient operator which is taken with respect to the subscript variable. For the TM case, $\bar{\bar{G}}(\boldsymbol{p},\boldsymbol{q})=G(\boldsymbol{p},\boldsymbol{q})\hat{z}\hat{z}$. Note that the data equation is nonlinear with respect to the unknown contrast as the electric field $\boldsymbol{E}$ inside the imaging domain is a function of χ. That is, the electric field inside the imaging domain is given via the domain equation,

$$\boldsymbol{E}(\boldsymbol{q})=\boldsymbol{E}^{\mathrm{inc}}(\boldsymbol{q})+k_b^2\int_{\mathcal{D}}\bar{\bar{G}}(\boldsymbol{q},\boldsymbol{q}')\cdot\chi(\boldsymbol{q}')\boldsymbol{E}(\boldsymbol{q}')d\boldsymbol{q}' \tag{4}$$

where $\boldsymbol{q}\in\mathcal{D}$. The inverse scattering problem may then be formulated as the minimization over χ of the least-squares data misfit cost-functional,

$$\mathcal{C}^{\mathcal{LS}}(\chi)=\frac{1}{\|\boldsymbol{E}^{\mathrm{meas}}(\cdot)\|_{\mathcal{S}}^2}\left\|\boldsymbol{E}^{\mathrm{scat}}(\cdot,\chi)-\boldsymbol{E}^{\mathrm{meas}}(\cdot)\right\|_{\mathcal{S}}^2 \tag{5}$$

where $\boldsymbol{E}^{\mathrm{meas}}(\cdot)$ denotes the measured scattered field on $\mathcal{S}$ and $\|\cdot\|_{\mathcal{S}}$ denotes the L_2-norm on $\mathcal{S}$.

It should be mentioned that for the TE inversion, we can also use the magnetic field integral equation which can be derived by taking the curl of both sides of (2) with respect to $\boldsymbol{p}$. However, we do not use the magnetic field formulation for the inversion as it has been shown in [20] that the TE inversion using the electric field formulation is more stable and has better performance than that using the magnetic field formulation.

Herein, we consider a discrete nonlinear inverse scattering problem where the number of measured data is limited, say M, and the imaging domain $\mathcal{D}$ is discretized into N cells using 2D pulse functions. Therefore, the measured scattered data on the discrete measurement domain $\mathcal{S}$ is denoted by the complex vector $\underline{E}^{\mathrm{meas}}\in\mathbb{C}^M$ and the contrast function is represented by the complex vector $\underline{\chi}\in\mathbb{C}^N$. We further assume that in the TE case the vector $\underline{E}^{\mathrm{meas}}$ is ordered in such a way that it contains the x-component of the measured scattered field, $\underline{E}_x^{\mathrm{meas}}\in\mathbb{C}^{M/2}$, at all observation points followed by the corresponding y-component, $\underline{E}_y^{\mathrm{meas}}\in\mathbb{C}^{M/2}$. However, in the TM case, the vector $\underline{E}^{\mathrm{meas}}$ consists only of the z-component of the measured scattered field, *i.e.,* $\underline{E}_z^{\mathrm{meas}}$. The discretized inverse scattering problem is formulated as the minimization of the least-squares data misfit

$$\mathcal{F}^{\mathcal{LS}}(\underline{\chi})=\frac{\left\|\underline{E}^{\mathrm{scat}}(\underline{\chi})-\underline{E}^{\mathrm{meas}}\right\|^2}{\left\|\underline{E}^{\mathrm{meas}}\right\|^2} \tag{6}$$

where $\underline{E}^{\mathrm{scat}}(\underline{\chi})$ represents the simulated scattered field vector at the measurement points due to the predicted contrast $\underline{\chi}$ and $\|.\|$ denotes the L_2-norm on $\mathbb{C}^M$.

III. Gauss-Newton Inversion Method

The Gauss-Newton Inversion (GNI) method is based on Gauss-Newton optimization [36] where the nonlinear cost-functional is approximated with a quadratic form at the current iteration that ignores the second-order derivatives. The stationary point of the quadratic model is then chosen as the next iterate. Herein, the cost-functional to be minimized is chosen to be an additive-multiplicatively regularized form of the data misfit $\mathcal{F}^{\mathcal{LS}}$, (6), to overcome the ill-posedness of the inverse scattering problem. That is, we apply the GNI method to the following cost-functional [5], [37], [38],

$$\mathcal{F}(\underline{\chi})=\mathcal{F}^{\mathcal{LS}}(\underline{\chi})\left[1+\alpha\mathcal{F}^{\mathcal{R}}(\underline{\chi})\right]. \tag{7}$$

where $\mathcal{F}^{\mathcal{R}}(\cdot)$ is the regularizer and α is a small positive parameter which is determined by the user in an *ad hoc* way. The regularizer is chosen to be the L_2-norm total variation of the contrast vector over the imaging domain. That is, $\mathcal{F}^{\mathcal{R}}(\cdot)$ is the discrete form of the cost-functional

$$\mathcal{C}^{\mathcal{R}}(\chi)=\frac{1}{A}\int_{\mathcal{D}}\left|\nabla_{\boldsymbol{q}}\chi(\boldsymbol{q})\right|^2d\boldsymbol{q} \tag{8}$$

where A is the area of the imaging domain. We then minimize (7) using the Gauss-Newton method and the contrast vector at iteration n is updated as

$$\underline{\chi}_{n+1}=\underline{\chi}_n+\nu_n\Delta\underline{\chi}_n. \tag{9}$$

Here the step-length ν_n is a real positive number which is determined using a line search algorithm described below. The Gauss-Newton correction $\Delta\underline{\chi}_n$ is found as in [5] by solving

$$\left(\boldsymbol{J}_n^H\boldsymbol{J}_n-\lambda_n\boldsymbol{\Sigma}\right)\Delta\underline{\chi}_n=\boldsymbol{J}_n^H\left(\underline{E}^{\mathrm{meas}}-\underline{E}_n^{\mathrm{scat}}\right)+\lambda_n\boldsymbol{\Sigma}\underline{\chi}_n \tag{10}$$

where $\underline{E}_n^{\mathrm{scat}}$ is the simulated scattered field vector at the observation points due to the contrast $\underline{\chi}_n$. The matrix $\boldsymbol{J}_n$ denotes the Jacobian matrix containing the derivative of $\underline{E}_n^{\mathrm{scat}}$ with respect to $\underline{\chi}$ and evaluated at $\underline{\chi}_n$. The superscript H stands for the complex conjugate transpose. The matrix $\boldsymbol{\Sigma}$ represents the discrete form of $(1/A)\nabla^2$ where ∇^2 represents the Laplacian operator. Assuming that the contrast function is zero on the boundary of $\mathcal{D}$, the matrix $\boldsymbol{\Sigma}$ is a negative definite matrix [38]. Therefore, the matrix $\boldsymbol{J}_n^H\boldsymbol{J}_n-\lambda_n\boldsymbol{\Sigma}$ represents a positive definite matrix; thus,

ensuring a descent direction for the Gauss-Newton correction [5], [36]. The positive parameter λ_n is calculated as

$$\lambda_n = \frac{\alpha \left\| \underline{E}^{\text{meas}} - \underline{E}_n^{\text{scat}} \right\|^2}{1 + \alpha \mathcal{F}^{\mathcal{R}}(\underline{\chi}_n)}. \tag{11}$$

Note that the regularization weight is controlled by λ_n in (10) and that as λ_n decreases throughout the iterations, because $\left\| \underline{E}^{\text{meas}} - \underline{E}_n^{\text{scat}} \right\|$ is minimized, the regularization is lessened; thus, providing an adaptive regularization [38], [39] for the inversion algorithm. The details of the algorithm are not presented here but are available in [5].

The step-length ν_n is determined using a line search algorithm and is based on that described in [8] and [10]. In this line search algorithm, we start with the full step, *i.e.,* $\nu_n = 1$, and check whether it satisfies,

$$\mathcal{F}(\underline{\chi}_n + \nu_n \Delta \underline{\chi}_n) \leq \mathcal{F}(\underline{\chi}_n) + \beta \nu_n \delta \mathcal{F}_n \tag{12}$$

where β is a small positive number (set to be 10^{-4}) and $\delta \mathcal{F}_n$ is the decrease rate of $\mathcal{F}(\underline{\chi})$ at $\underline{\chi}_n$ in the direction of $\Delta \underline{\chi}_n$. If ν_n satisfies (12), we choose it as an appropriate step-length; otherwise we reduce the step-size along $\Delta \underline{\chi}_n$ until we find a ν_n which satisfies (12). In this procedure, the function $g(\nu) \triangleq \mathcal{F}(\underline{\chi}_n + \nu \Delta \underline{\chi}_n)$ is approximated by a quadratic expression in terms of ν and a new candidate for the step-length is then found by minimizing this quadratic form. As in [8], the minimum possible value for ν is set to 0.1. If the step-length becomes less than 0.1, we choose $\nu = 0.1$ and terminate the line search algorithm.

The inversion algorithm terminates if one of the following three conditions is satisfied: *(i)* the data misfit $\mathcal{F}^{\mathcal{LS}}$ is less than a prescribed error (set to be 10^{-3}), *(ii)* the difference between two successive data misfits becomes less than a prescribed value (set to be 10^{-4}), or *(iii)* the total number of iterations exceeds a prescribed maximum (set to be 50 for the single-frequency inversion).

IV. The Forward Solver

In each iteration of the GNI algorithm, the forward solver is called several times to compute the simulated scattered field at the observation points and its derivative with respect to the current estimate of the contrast. In addition, the line search algorithm requires calling the forward solver to evaluate (12). Therefore, having a fast forward solver is essential for this inversion algorithm. The forward solver is concerned with solving a linear well-posed system of equations which is solved using the Conjugate Gradient (CG) technique and accelerated using the Fast Fourier Transform (FFT). This is possible because of the convolutionary form of the domain operator when the imaging domain $\mathcal{D}$ is discretized uniformly using pulse basis functions in the x and y directions. To accomplish a CG-FFT forward solver, a procedure similar to [16] is adopted where the domain equation, (4), is formulated in terms of the so-called contrast sources, defined as $\boldsymbol{W}(\boldsymbol{q}) = \chi(\boldsymbol{q})\boldsymbol{E}(\boldsymbol{q})$. This can be done by multiplying (4) by the contrast and formulating the domain equation in terms of the contrast sources as

$$(\mathcal{I} - \chi \mathcal{G}_{\mathcal{D}})\boldsymbol{W} = \chi \boldsymbol{E}^{\text{inc}} \tag{13}$$

where $\mathcal{I}$ denotes the identity operator and $\mathcal{G}_{\mathcal{D}}$ is defined as

$$\mathcal{G}_{\mathcal{D}}(\boldsymbol{W}) \triangleq k_b^2 \int_{\mathcal{D}} \bar{\bar{G}}(\boldsymbol{q}, \boldsymbol{q}') \cdot \boldsymbol{W}(\boldsymbol{q}') d\boldsymbol{q}'. \tag{14}$$

After finding the contrast sources from the discrete form of (13) using the CG-FFT algorithm, the total field inside $\mathcal{D}$ can be simply calculated from

$$\boldsymbol{E}(\boldsymbol{q}) = \boldsymbol{E}^{\text{inc}}(\boldsymbol{q}) + \mathcal{G}_{\mathcal{D}}(\boldsymbol{W}). \tag{15}$$

To further accelerate the forward solver, we have used the marching-on-in-source-position technique [5], [40] where an appropriate initial guess for the CG-FFT algorithm with respect to a specific transmitter position is obtained via an extrapolation of the fields corresponding to some previous transmitter positions. In this paper, the initial guess for the mth transmitter $(m \geq 4)$ to be used in the CG-FFT algorithm applied to the discrete form of (13) is written as

$$\boldsymbol{W}_m^0(\boldsymbol{q}) = \sum_{t=1}^{3} \zeta_t \boldsymbol{W}_{m-t}(\boldsymbol{q}) \tag{16}$$

where $\boldsymbol{W}_{m-t}(\boldsymbol{q})$ is the converged solution of (13) with respect to $(m-t)^{\text{th}}$ transmitter. A closed-form expression for the coefficients ζ_t is available such that they minimize the following norm [5],

$$\left\| (\mathcal{I} - \chi \mathcal{G}_{\mathcal{D}}) \boldsymbol{W}_m^0 - \chi \boldsymbol{E}_m^{\text{inc}} \right\|_{\mathcal{D}} \tag{17}$$

where $\|.\|_{\mathcal{D}}$ denotes the L_2-norm on $\mathcal{D}$. For the first three transmitters, we have used a zero initial guess.

V. Theoretical Computational Complexity Analysis

A description of the per-iteration computational complexity of the utilized TE and TM GNI algorithms is now given. The following conventions are used: the number of transmitters is denoted by T_x, the total number of receiver positions by R_x, and the number of receiver positions per transmitter by R. The number of CG iterations required for the TE and TM forward solvers are denoted by F_{TE} and F_{TM}, respectively. The number of CG iterations to find the Gauss-Newton correction in the TE and TM cases are denoted by P_{TE} and P_{TM}, respectively. The contrast function χ is discretized on a uniform grid using 2D pulse functions Π_i, $i = 1 \ldots N$ and denoted by the contrast vector $\underline{\chi}$ whose ith component is represented by $[\underline{\chi}]_i$.

A. Jacobian Matrix

Each row of the Jacobian matrix $\boldsymbol{J}$ will correspond to a combination of the scattered field at a receiver located at, say, $\boldsymbol{p}$ and

polarized along some direction, say, $\hat{\tau}$ and due to one transmitter, say, the tth transmitter. That is, one row for each individual datum of the collected data. The ordering of the rows will obviously depend on the ordering of this data, but the ith element in such a row will correspond to the derivative of this scattered field with respect to $[\underline{\chi}]_i$. This element may be found using an adjoint formulation [41] as [5], [8]

$$k_b^2 \int_{\mathcal{D}} \Pi^i(\boldsymbol{q}) \boldsymbol{E}_t(\boldsymbol{q}) \cdot \bar{\bar{G}}^{\text{inh}}(\boldsymbol{q}, \boldsymbol{p}) \cdot \hat{\tau} d\boldsymbol{q}. \tag{18}$$

In the TE case, $\bar{\bar{G}}^{\text{inh}}(\boldsymbol{q}, \boldsymbol{p})$ is the dyadic Green's function for the inhomogeneous background, which is the predicted scatterer at the current GNI iteration, evaluated at the point $\boldsymbol{q}$ due to the source at the point $\boldsymbol{p}$ (also called the distorted dyadic Green's function). In the TM case, $\bar{\bar{G}}^{\text{inh}} = G_{zz}^{\text{inh}} \hat{z}\hat{z}$ where G_{zz}^{inh} is the 2D scalar Green's function for the inhomogeneous background. Also, $\boldsymbol{E}_t(\boldsymbol{q})$ is the total field inside the imaging domain due to the t^{th} transmitter and corresponding to the predicted contrast. For our cases, the polarization direction $\hat{\tau}$ is considered to be either $\hat{x}$ or $\hat{y}$ in the TE case and $\hat{z}$ in the TM case.

Finding the distorted dyadic Green's function for the R_x different receiver positions requires calling the forward solver $2R_x$ times in the TE case and R_x times in the TM case. This is due to the fact that two different polarizations should be considered in the TE illumination while only one polarization is needed for the TM illumination. The computational cost for finding $\boldsymbol{E}_t(\boldsymbol{q})$ for different transmitter locations is T_x calls of the forward solver for both TE and TM cases as the TE-polarized data is calibrated (or synthetically created) using an infinite magnetic line source directed in $\hat{z}$ direction.

In our implementation, the elements of the matrix $\boldsymbol{J}$, as given in (18), are not found explicitly as we only need to do the right matrix-vector multiplication using $\boldsymbol{J}$ and $\boldsymbol{J}^H$, see (10). Therefore, the integration and the dot-product $\boldsymbol{E}_t \cdot \bar{\bar{G}}_{\text{inh}}$, as required in (18), is computed when $\boldsymbol{J}$ (or $\boldsymbol{J}^H$) operates on a vector of the proper size and will be considered in the computational complexity of finding the Gauss-Newton correction.

B. The Gauss-Newton Correction

Solving $\Delta\underline{\chi}_n$ in (10) using CG requires multiplying $\boldsymbol{J}^H\boldsymbol{J}$ by a vector and this requires approximately $8RT_xN$ multiplications in the TE case and $2RT_xN$ multiplications in the TM case. This can be explained as follows: in the TE case, the multiplication of the Jacobian matrix $\boldsymbol{J}$ with a vector $\underline{r} \in \mathbb{C}^{N\times 1}$ can be written as,

$$\boldsymbol{J}\underline{r} = \begin{pmatrix} \boldsymbol{G}_{xx}^{\text{inh}}(\underline{E}_x \odot \underline{r}) + \boldsymbol{G}_{yx}^{\text{inh}}(\underline{E}_y \odot \underline{r}) \\ \boldsymbol{G}_{xy}^{\text{inh}}(\underline{E}_x \odot \underline{r}) + \boldsymbol{G}_{yy}^{\text{inh}}(\underline{E}_y \odot \underline{r}) \end{pmatrix} \tag{19}$$

and in the TM case as

$$\boldsymbol{J}\underline{r} = \boldsymbol{G}_{zz}^{\text{inh}}(\underline{E}_z \odot \underline{r}) \tag{20}$$

where $\boldsymbol{G}_{\varsigma\eta}^{\text{inh}}$ represents the matrix form of the $\hat{\varsigma}\hat{\eta}$-component of the distorted dyadic Green's function. The operation $\odot$ denotes the elementwise product (Hadamard product) of two conforming vectors. Using (19) and (20), it can be concluded that the matrix-vector multiplication $\boldsymbol{J}\underline{r}$ requires approximately $4RT_xN$ operations in the TE case and R_xTN operations in the TM case. The same conclusion can be drawn for multiplying the matrix $\boldsymbol{J}^H$ by an arbitrary vector of the correct size. Therefore, the computational cost of calculating $\boldsymbol{J}_n^H\boldsymbol{J}_n\Delta\underline{\chi}_n$, as required in (10), is about $8RT_xN$ in the TE case and $2RT_xN$ in the TM case.

The matrix $\boldsymbol{\Sigma}$ for a rectangular imaging domain is a symmetric block Toeplitz matrix with Toeplitz blocks [42, p. 100], so its multiplication with a vector can be accelerated using the FFT; thus, the computational cost of $\boldsymbol{\Sigma}\Delta\underline{\chi}_n$ is neglected compared to that of $\boldsymbol{J}_n^H\boldsymbol{J}_n\Delta\underline{\chi}_n$. Therefore, the computational cost for finding the Gauss-Newton correction is about $2P_{\text{TE}} \times (8RTN)$ for the TE case and $2P_{\text{TM}} \times (2RTN)$ for the TM case. Note that each iteration of the CG algorithm requires two matrix-vector multiplications. Assuming $P_{\text{TE}} \approx P_{\text{TM}}$, the computational complexity of finding the correction in the TE case is almost four times more than that in the TM case.

C. The Forward Solver

The CG-FFT forward solver, applied to the discrete form of (13), requires the definition of the $(\mathcal{I} - \chi\mathcal{G}_{\mathcal{D}})$ operator and its adjoint. In the TE case, this operator may be defined as [16]

$$\begin{aligned}(\mathcal{I} - \chi\mathcal{G}_{\mathcal{D}})\boldsymbol{W} = &\left(W_x - \chi\left[k_b^2 A_x + B_x\right]\right)\hat{x} \\ &+ \left(W_y - \chi\left[k_b^2 A_y + B_y\right]\right)\hat{y}\end{aligned} \tag{21}$$

and in the TM case, as

$$(\mathcal{I} - \chi\mathcal{G}_{\mathcal{D}})\boldsymbol{W} = \left(W_z - \chi k_b^2 A_z\right)\hat{z} \tag{22}$$

where W_ς is the $\hat{\varsigma}$ component of $\boldsymbol{W}$. Also, A_ς and B_ς are defined as

$$A_\varsigma(\boldsymbol{q}) = \int_{\mathcal{D}} G(\boldsymbol{q}, \boldsymbol{q}') W_\varsigma(\boldsymbol{q}') d\boldsymbol{q}', \tag{23}$$

$$B_\varsigma(\boldsymbol{q}) = \hat{\varsigma} \cdot (\nabla_{\boldsymbol{q}} \nabla_{\boldsymbol{q}} \cdot [A_x(\boldsymbol{q})\hat{x} + A_y(\boldsymbol{q})\hat{y}]). \tag{24}$$

As pointed out in [16], the discrete forms of both A_ς and B_ς can be computed by FFT routines. The discrete form of A_ς may be computed by multiplying a symmetric block Toeplitz matrix with Toeplitz blocks with W_ς. However, the discrete form of B_ς can be computed by multiplying a symmetric Toeplitz matrix with A_x and A_y. Due to the fact that the matrix-vector multiplication by a symmetric block Toeplitz matrix with Toeplitz blocks is more expensive than that by a symmetric Toeplitz matrix [43], we ignore the computational complexity of finding B_ς compared to that of finding A_ς. Using this approximation, the computational cost of multiplying the discrete form of $(\mathcal{I} - \chi\mathcal{G}_{\mathcal{D}})$ by an arbitrary vector of the correct size in the TE case is roughly two times of that in the TM case as the TE forward solver requires the calculation of A_x and A_y whereas the TM forward solver only requires the calculation of A_z.

Using the above approximation, it can also be shown that the computational complexity of multiplying the discrete form of the adjoint operator of $(\mathcal{I} - \chi\mathcal{G}_{\mathcal{D}})$ with an arbitrary vector of

the correct size in the TE case is also two times of that in the TM case. Therefore, the per-iteration computational complexity of the TE CG-FFT algorithm, utilized in the forward solver, is roughly twice that of the TM case.

D. Line Search

The computational cost of the utilized line search algorithm is approximately equal to that of evaluating $\mathcal{F}(\underline{\chi}_n + \nu\Delta\underline{\chi}_n)$ for the known background Green's function and this is equal to calling the forward solver T_x times for both TE and TM cases. As mentioned earlier, if the full step satisfies the condition (12), we choose it as an appropriate step-length. From our experience with the regularized cost functional (7), the full step mostly satisfies the condition (12); therefore, very few calls to this line search algorithm are made in the cases that we have run. This can be explained as follows. In the Gauss-Newton optimization, the correction $\Delta\underline{\chi}_n$ may lead to an increase in the cost-functional if (i) $\boldsymbol{J}_n^H\boldsymbol{J}_n - \lambda_n\boldsymbol{\Sigma}$, see (10), is not positive-definite, or (ii) the quadratic model of the nonlinear regularized cost-functional $\mathcal{F}(\underline{\chi})$ at $\underline{\chi}_n$ is not a *good* approximation to $\mathcal{F}(\underline{\chi})$[4]. As pointed out in Section III, the matrix $\boldsymbol{J}_n^H\boldsymbol{J}_n - \lambda_n\boldsymbol{\Sigma}$ is positive definite. Moreover, due to the use of adaptive regularization, the regularization weight λ_n is maximum at early GNI iterations where the predicted contrast can be very far from the true solution. Thus, at early GNI iterations, the quadratic model of $\mathcal{F}(\underline{\chi})$ is dominated by that of the regularizer. Noting that the regularizer is an L_2-norm, the quadratic model of the regularized cost-functional has a good chance to be a good approximation of $\mathcal{F}(\underline{\chi})$ at early GNI iterations. As the algorithm gets closer to the true solution, the regularization weight λ_n is lessened. Thus, the quadratic model of the regularized cost-functional is dominated by that of the data misfit functional. Due to the fact that the predicted contrast is close to the true solution, the quadratic model of the regularized cost-functional has a good chance to be a good approximation of $\mathcal{F}(\underline{\chi})$. Therefore, the use of adaptive regularization will usually make the quadratic model of the regularized cost-functional be a good approximation to $\mathcal{F}(\underline{\chi})$.

VI. Inversion Results

The inversion results from both synthetic and experimental data are now shown. To be able to compare the TE inversion with the TM inversion, we introduce an image error cost-functional defined as

$$\mathcal{M}(\underline{\chi}) = \frac{\left\|\underline{\chi} - \underline{\chi}^{\text{true}}\right\|^2}{\left\|\underline{\chi}^{\text{true}}\right\|^2} \tag{25}$$

where $\underline{\chi}$ is the final reconstruction, $\underline{\chi}^{\text{true}}$ is the true contrast and $\|.\|$ denotes the L_2-norm on $\mathbb{C}^N$. For the experimental data, $\underline{\chi}^{\text{true}}$ is created according to the geometrical configurations and the average permittivity of the object being imaged. For the synthetic data, as the data is generated on a different grid than the one used in the GNI algorithm (to avoid inverse crime), the image error cost-functional (25) is calculated by interpolating onto a finer and finer mesh until the norm converged. For the synthetic data sets, all parameters of the forward solver are kept the same for TE and TM polarizations. We have also added 3% RMS additive white noise to the synthetic data set using the formula given in [44].

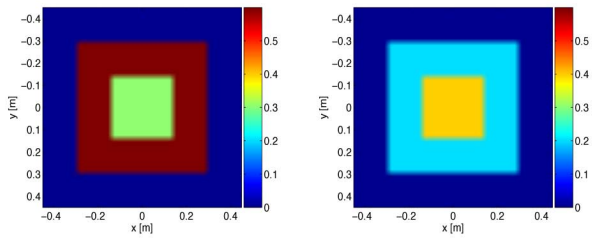

(a) $Real(\chi)$ (b) $Imag(\chi)$

Fig. 2. The exact contrast of the scatterer for the synthetic test case. (a) $Real(\chi)$. (b) $Imag(\chi)$.

A. Synthetic Data: Concentric Squares

We consider a similar test case which has been used in [15], [20], [45]. The scatterer consists of two concentric squares with an inner square having dimension of $\lambda_b \times \lambda_b$ (λ_b is the wavelength in the background medium) with a contrast of $0.3 + j0.4$. The inner square is surrounded by an exterior square having sides of $2\lambda_b$ and contrast $\chi = 0.6 + j0.2$. The exact contrast profile is shown in Fig. 2. The frequency of operation is chosen to be 1 GHz and free space is assumed for the background medium. The imaging domain $\mathcal{D}$ consists of a square having sides of $3\lambda_b$. We consider three different scenarios for collecting the data. In the first scenario, we choose 10 transmitters and 10 receivers ($R_x = R = 10$) on the measurement circle $\mathcal{S}$ and in the second scenario, we choose 30 transmitters and 30 receivers ($R_x = R = 30$) on $\mathcal{S}$. Therefore, the length of the vector $\underline{E}^{\text{meas}}$ in the second scenario is 9 times that of $\underline{E}^{\text{meas}}$ in the first scenario. In these two scenarios, the transmitters and receivers are placed evenly on the measurement circle $\mathcal{S}$ of radius $2.33\lambda_b = 70\text{cm}$. In the third scenario, we choose 10 transmitters and 10 receivers ($R_x = R = 10$) evenly placed on the measurement circle $\mathcal{S}$ of radius $10\lambda_b = 300$ cm. The forward data is then generated on a grid of 30×30 for both TE and TM polarizations. The transmitters for the TE and TM cases are the magnetic line source and electric line source respectively. For the TE case, E_x and E_y components are collected at the receiver positions whereas in the TM case, the E_z component is collected. We will note that the synthetically collected data in the first and second scenarios may be considered as the near-field data whereas the collected data in the third scenario is at far-field.

For the first scenario, the TE and TM inversions are shown in Fig. 3. As can be seen, both TE and TM inversions provide good reconstructions for the real part of the contrast profile. However, the TM inversion is not successful in reconstructing the imaginary part of the contrast: the inner square is unresolved in the imaginary part of the TM inversion. It should be noted that when the number of transmitters/receivers decreased to 8, the TE inversion also failed (not shown here) in reconstructing this target. The TE and TM inversions for the second scenario are shown in Fig. 4. In this case, both TE and TM inversions are successful in reconstructing real and imaginary parts of the contrast. For the third scenario which utilizes the same number of transmitters

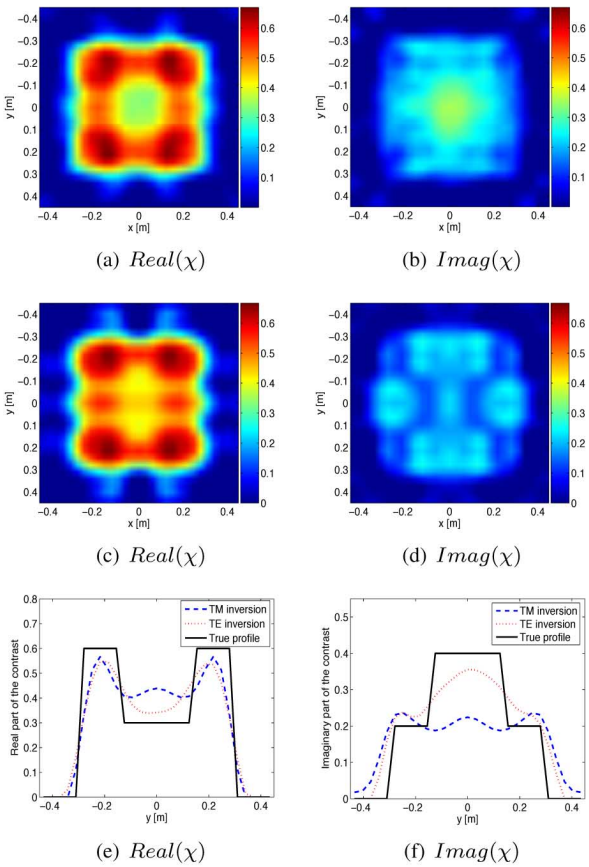

Fig. 3. Inversion of the synthetic data set (the first scenario: $T_x = 10$ and $R = R_x = 10$) (a)–(b) TE case (c)–(d) TM case (e)–(f) cross-section at $x = 0$. (a) $Real(\chi)$. (b) $Imag(\chi)$. (c) $Real(\chi)$. (d) $Imag(\chi)$. (e) $Real(\chi)$. (f) $Imag(\chi)$.

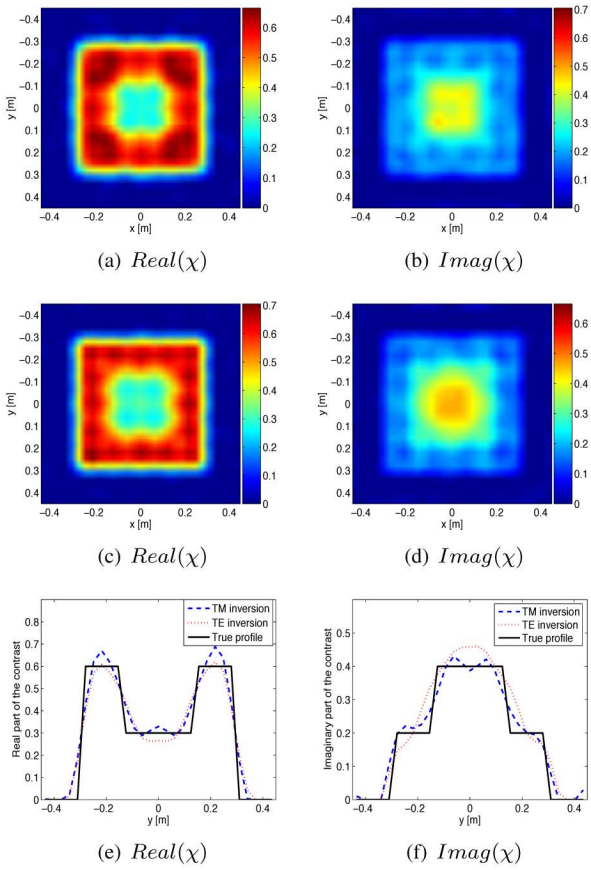

Fig. 4. Inversion of the synthetic data set (the second scenario: $T_x = 30$ and $R = R_x = 30$) (a)–(b) TE case (c)–(d) TM case (e)–(f) cross-section at $x = 0$. (a) $Real(\chi)$. (b) $Imag(\chi)$. (c) $Real(\chi)$. (d) $Imag(\chi)$. (e) $Real(\chi)$. (f) $Imag(\chi)$.

and receivers as in the first scenario but located in far-field, the TE and TM inversions are shown in Fig. 5. In this case, the TE and TM inversions are very similar. The number of GNI iterations utilized to reconstruct this target and the value of $\mathcal{M}(\underline{\chi})$ in these three different scenarios are given in Tables I and II.

That the TE inversion outperforms the TM inversion in the first scenario is probably due to the fact that the TE near-field data contains more information than the TM near-field data (the length of the vector $\underline{E}^{\text{meas}}$ in the TE case is twice that in the TM case). Noting that the measurement circle $\mathcal{S}$ is in the near-field for this test case, it is expected that $\underline{E}_x^{\text{meas}}$ and $\underline{E}_y^{\text{meas}}$ provide non-redundant information. However, when the number of transmitters and receivers increases in the second scenario, the TM scattering data provides sufficient information to reconstruct the object with a reasonable accuracy while the TE inversion also provides a good reconstruction in this case. Comparing the inversion results for the first and third scenarios, we speculate that the TE far-field data does not provide extra information compared to the TM far-field data.

B. The Second Fresnel Experimental Data Set

For the second Fresnel data set [28], the transmitting and receiving antennas are both wide-band ridged horn antennas and are located on a circle with radius 1.67 m. The targets, see Fig. 6, are all long circular cylinders and have no variations in the longitudinal direction. Both TE and TM polarizations are measured for each target where the background medium is free space. In the TM illumination, the z-component of the total and incident electric fields are collected for different transmitter positions and frequencies. In the TE illumination, the φ-component of total and incident electric fields are measured (the $\hat{\varphi}$ direction is depicted in Fig. 1). The scattered field is obtained by subtracting the measured incident field from the measured total field. The scattered field is then calibrated by approximating the horn transmitting and receiving antennas by line transmitters and receivers (electric line source for TM illumination and magnetic line source for TE illumination). The calibration procedure adopted is that explained in [27] where a single calibration factor per transmitter is used: for each transmitter the calibration factor used is the ratio of the simulated incident field to the measured incident field for the receiver point opposite to the transmitter (this factor is used for all receiver points). Note that in the TE-polarized data provided by the Fresnel group, only one component of the electric field, i.e., E_φ, has been measured. This component is then calibrated and converted to E_x and E_y to be used by the inversion algorithm.

The *FoamDielInt* and *FoamDielExt* targets are illuminated by 8 transmitters and the measured data is collected at 9 different frequencies from 2 GHz to 10 GHz with a step of 1 GHz at

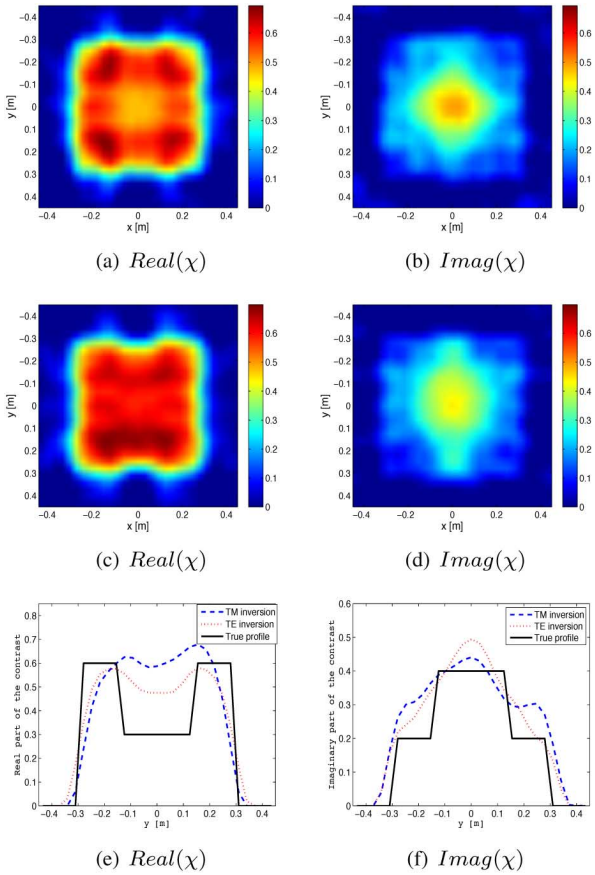

Fig. 5. Inversion of the synthetic data set (the third scenario: $T_x = 10$ and $R = R_x = 10$ and the transmitters/receivers are located in far-field) (a)–(b) TE case (c)–(d) TM case (e)–(f) cross-section at $x = 0$. (a) $Real(\chi)$. (b) $Imag(\chi)$. (c) $Real(\chi)$. (d) $Imag(\chi)$. (e) $Real(\chi)$. (f) $Imag(\chi)$.

TABLE I
NUMBER OF GNI ITERATIONS REQUIRED FOR THE CONVERGENCE (MULTIPLE-FREQUENCY INVERSION)

Target	TE case	TM case
Concentric squares (1st scenario)	6	6
Concentric squares (2nd scenario)	8	8
Concentric squares (3rd scenario)	5	6
FoamDielInt	14	21
FoamDielExt	15	27
FoamTwinDiel	19	36
FoamMetExt	19	25
FoamTwinDiel ($f = 6$ GHz)	7	25

241 points per transmitter. The *FoamTwinDiel* target is irradiated by 18 transmitters and the number of receivers and frequencies stays the same as two previous cases. For the *FoamMetExt* target, the numbers of transmitters and receivers are the same as those for *FoamTwinDiel* target but the object is illuminated at 17 different frequencies in the range of 2 GHz to 18 GHz with 1 GHz step. For all these targets, the imaging domain, $\mathcal{D}$, is a 15 cm $\times$ 15 cm square region which is discretized into a $N = 60 \times 60$ uniform grid. For the single-frequency inversion, we use $\underline{\chi} = 0$ as the initial guess to the GNI method and for the multiple-frequency inversions, the frequency-hopping approach [46] is used where the reconstructed image from low-frequency

TABLE II
IMAGE ERROR COST—FUNCTIONAL $\mathcal{M}(\underline{\chi})$

Target	TE case	TM case
Concentric squares (1st scenario)	0.10	0.15
Concentric squares (2nd scenario)	0.06	0.05
Concentric squares (3rd scenario)	0.14	0.16
FoamDielInt	0.13	0.14
FoamDielExt	0.16	0.18
FoamTwinDiel	0.20	0.18
FoamMetExt	0.23	0.29
FoamTwinDiel ($f = 6$ GHz)	0.22	0.20

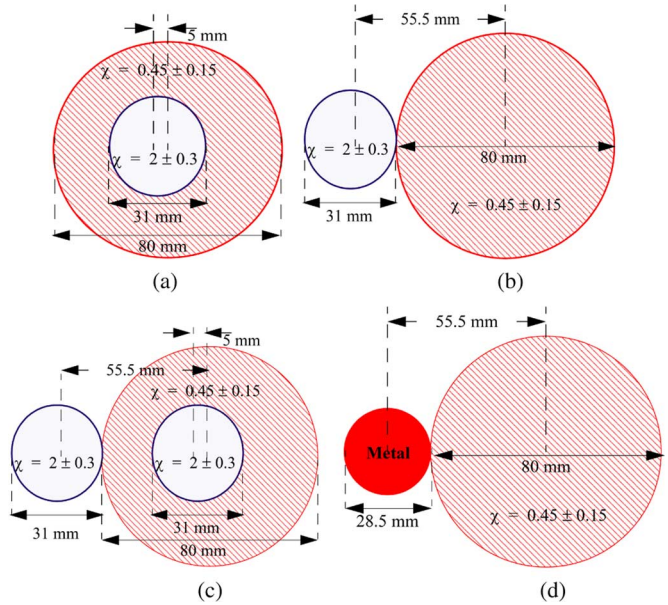

Fig. 6. The targets of the second Fresnel data set. (a) *FoamDielInt*. (b) *FoamDielExt*. (c) *FoamTwinDiel*. (d) *FoamMetExt*.

data is used as an initial guess for the inversion of high-frequency data. For the *FoamMetExt* target, we have limited the maximum value of the imaginary part to be 4 at $f = 2$ GHz as otherwise the imaginary part of the metal cylinder will become too high (on the order of 200), making the convergence of the forward solver difficult. Therefore, if the imaginary part of the contrast of this target becomes more than four, it is set to four.

1) Multiple-Frequency Inversion: The multiple-frequency inversion results for the Fresnel targets are shown in Figs. 7–10. For all these four targets, the TE and TM inversions have been successful in reconstructing the targets with a reasonable accuracy. For the *FoamDielInt*, *FoamDielExt* and *FoamTwinDiel*, the reconstructed imaginary parts of both TE and TM inversions are small which indicates that these three targets are lossless. For the *FoamMetExt* target, it can be seen that the shape of the dielectric cylinder is reconstructed well in the TE case whereas its shape in the proximity of the metallic cylinder is not reconstructed in the TM case. Also, for both polarizations the reconstructed real part of the metallic cylinder is close to zero whereas the imaginary part is indicated to be an object of high loss. The number of GNI iterations required to reconstruct these objects is listed in Table I which shows a faster convergence for the TE inversion of the Fresnel targets. The value of the image

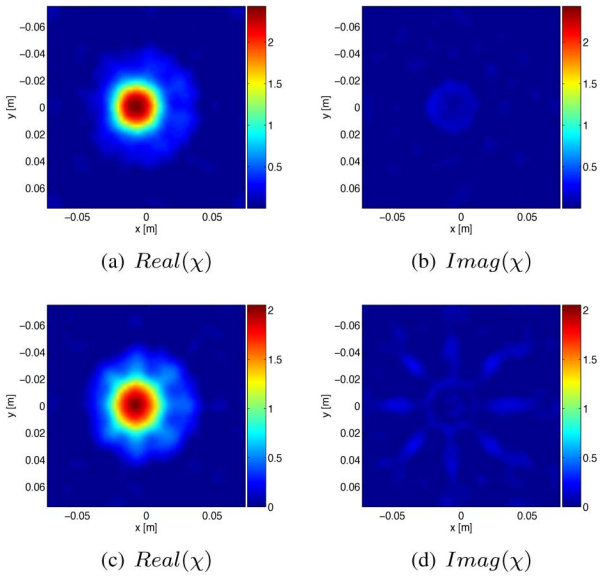

Fig. 7. *FoamDielInt* reconstruction (a)–(b) TE case (c)–(d) TM case. (a) $Real(\chi)$. (b) $Imag(\chi)$. (c) $Real(\chi)$. (d) $Imag(\chi)$.

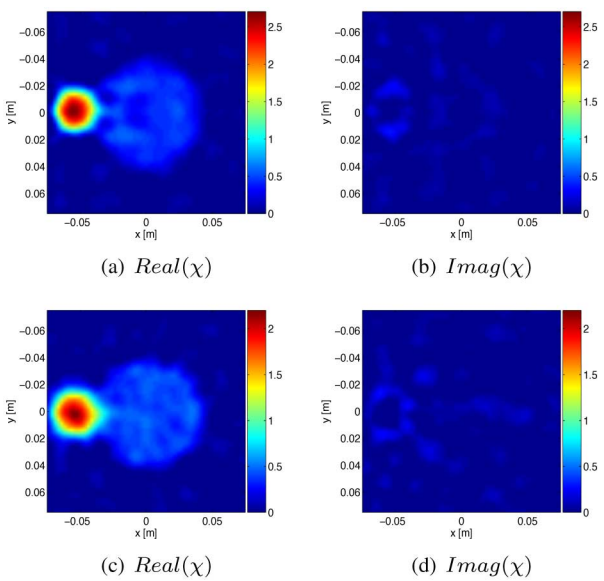

Fig. 8. *FoamDielExt* reconstruction (a)–(b) TE case (c)–(d) TM case. (a) $Real(\chi)$. (b) $Imag(\chi)$. (c) $Real(\chi)$. (d) $Imag(\chi)$.

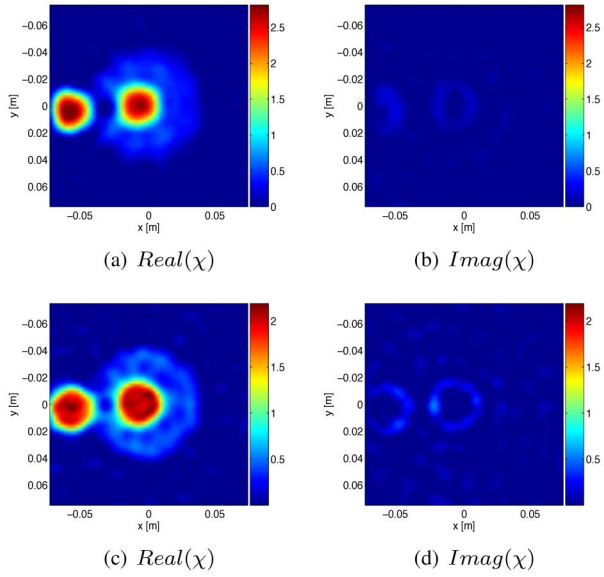

Fig. 9. *FoamTwinDiel* reconstruction (a)–(b) TE case (c)–(d) TM case. (a) $Real(\chi)$. (b) $Imag(\chi)$. (c) $Real(\chi)$. (d) $Imag(\chi)$.

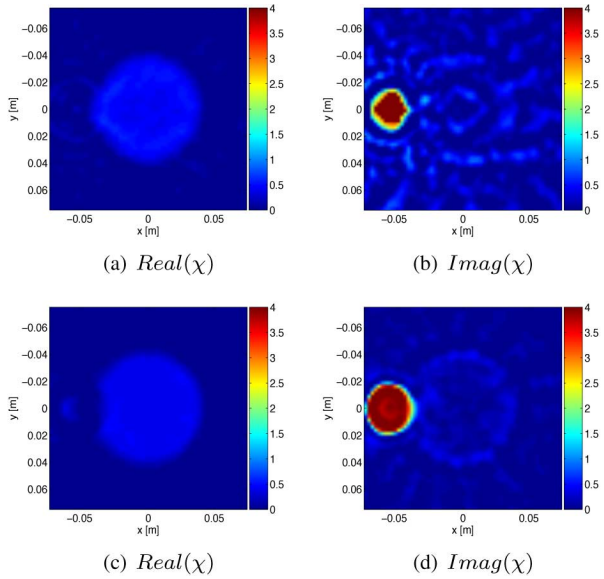

Fig. 10. *FoamMetExt* reconstruction (a)–(b) TE case (c)–(d) TM case. (a) $Real(\chi)$. (b) $Imag(\chi)$. (c) $Real(\chi)$. (d) $Imag(\chi)$.

error cost-functional $\mathcal{M}(\underline{\chi})$ for TE and TM inversions of these targets is given in Table II which shows a relatively similar reconstructions for the TE and TM inversions.

2) Single-Frequency Inversion: To investigate the single-frequency inversion of the experimental Fresnel data for the TE case, we show the reconstruction results of *FoamTwinDiel* target at $f = 6$ GHz and compare it to the TM inversion at the same frequency. In both TE and TM inversions, we start the inversion algorithm with $\underline{\chi} = 0$ as the initial guess. The algorithm converged after 7 iterations for the TE case and 25 iterations for the TM case. The data misfit $\mathcal{F}^{\mathcal{LS}}$ for the first iteration was 0.3803 for the TE case and 0.3809 for the TM case. However, in the final reconstruction, the data misfit reduced to 0.0285 for the TE case and 0.0266 for the TM case. The data misfit for different iterations of the inversion algorithm for both TE and TM inversions is shown in Fig. 11. The TE inversion, Fig. 12(a)–(b), overshoots the real part of the contrast for the external cylinder while the TM inversion, Fig. 12(c)–(d), is very close to the true contrast. The value of the image error cost-functional for the single-frequency TE and TM inversions of the *FoamTwinDiel* is given in Table II.

As far as the computational complexity of the TE and TM inversions is concerned, the inversion codes have been written in object-oriented Matlab and all the computations are performed on a computer with a quad-core 2.66 GHz Intel processor and 2 GB of RAM. As an example, we consider the *FoamDielInt* target where $T = 8$, $R_x = 360$, $R = 241$ and $N = 3600$. In the first

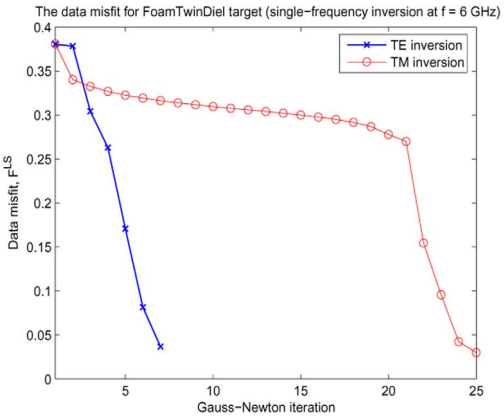

Fig. 11. The data misfit $\mathcal{F}^{\mathcal{LS}}$ for the single-frequency inversion of the *FoamTwinDiel* target at $f = 6$ GHz.

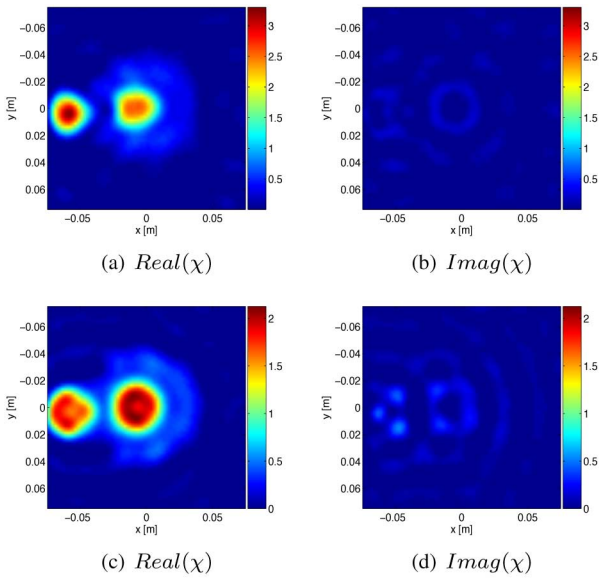

Fig. 12. Single-frequency reconstruction of *FoamTwinDiel* at $f = 6$ GHz (a)–(b) TE case (c)–(d) TM case. (a) $Real(\chi)$. (b) $Imag(\chi)$. (c) $Real(\chi)$. (d) $Imag(\chi)$.

GNI iteration at $f = 2$ GHz we have $F_{\mathrm{TE}} = 12$ and $P_{\mathrm{TE}} = 50$ for the TE case whereas in the TM case, $F_{\mathrm{TM}} = 9$ and $P_{\mathrm{TM}} = 48$. Finding the Gauss-Newton correction took about 320 sec for the TE case and 79 sec for the TM case. That is, finding the correction in the TE case is about 4 times more expensive than that in the TM case which matches the expected theoretical ratio. Also, for each transmitter, the forward solver took about 0.99 sec in the TE case and 0.31 sec in the TM case showing that the per-iteration computational complexity of the TE forward solver is about 2.4 times more than that of the TM case which is very close to the approximate theoretical ratio. Also, in the inversion of the *FoamDielInt* target, the line search algorithm was called once for each frequency in both polarizations.

The computational cost can be significantly alleviated by using the marching-on-in-source-position technique [5], [40] which essentially reduces F_{TE} and F_{TM}. For example, in the first GNI iteration for the *FoamDielInt* target at $f = 2$ GHz, it took about 691 sec for the TE case and 114 sec for the TM case to find the inhomogeneous Green's function without using the marching-on-in-source-position technique. However, the update procedure took just 295 sec for the TE case and 53 sec for the TM case when this technique was used.

It is important to note that for experimental tomographic systems where the receiver positions are the same as transmitter positions, which is the case for most practical microwave imaging systems currently in existence, computational savings can be made in updating the Green's function of the inhomogeneous background using the already updated total field corresponding to each transmitter.

VII. The Gauss-Newton Inversion With a Krylov Subspace Regularization Method

To verify that the above results are not due to the specific use of the additive-multiplicative regularization, we also use a Krylov subspace regularization method. Specifically, we use the conjugate gradient least squares (CGLS) regularization technique [7], [38], [47], as a Krylov regularization method, in conjunction with the GNI method. We will refer to this inversion algorithm as GNI-CGLS in this paper. We have three main reasons to use this specific regularization method. First, the CGLS regularization method provides a basic and simple regularization method. It can be shown that this regularization provides similar results to truncated singular value decomposition (TSVD) and standard-form Tikhonov regularization [42, pg. 50], [48, p. 146], [38], [49]; mainly due to the similarity between the Krylov subspace basis and the SVD basis. Second, the CGLS regularization provides computationally more efficient regularization compared to the TSVD and Tikhonov regularization. Third, an adaptive regularization parameter choice method for the CGLS regularization technique has been presented in [7] and successfully used for the inversion of experimental biomedical data such as the ones collected from human breast and forearm [7], [47].

The GNI-CGLS method was applied to the the first scenario of the synthetic data set and the inversion result is shown in Fig. 13. Similar to the inversion result using the GNI method with the additive-multiplicative regularizer shown in Fig. 3, the TE GNI-CGLS inversion outperforms the TM GNI-CGLS inversion. The TE GNI-CGLS inversion converged after 7 iterations whereas the TM GNI-CGLS inversion converged after 12 iterations. The image cost-functional $\mathcal{M}(\chi)$ is 0.08 for the TE GNI-CGLS inversion and 0.11 for the TM GNI-CGLS inversion. For the second and third scenarios of the synthetic data set as well as the Fresnel experimental data set, the inversion results from the GNI-CGLS method (not shown here) were very similar to those from the GNI method with the additive-multiplicative regularizer. Similar to the GNI method with the additive-multiplicative regularizer, the TE GNI-CGLS method requires equal or less iterations than the TM GNI-CGLS method. For example, for the single-frequency *FoamTwinDiel* case $(f = 6$ GHz$)$, the TE GNI-CGLS method converged after 15 iterations whereas the TM GNI-CGLS method converged after 27 iterations. The data misfit for different iterations of the GNI-CGLS method for both TE and TM polarizations is shown in Fig. 14. Similar to the GNI with the additive-multiplicative regularizer shown in

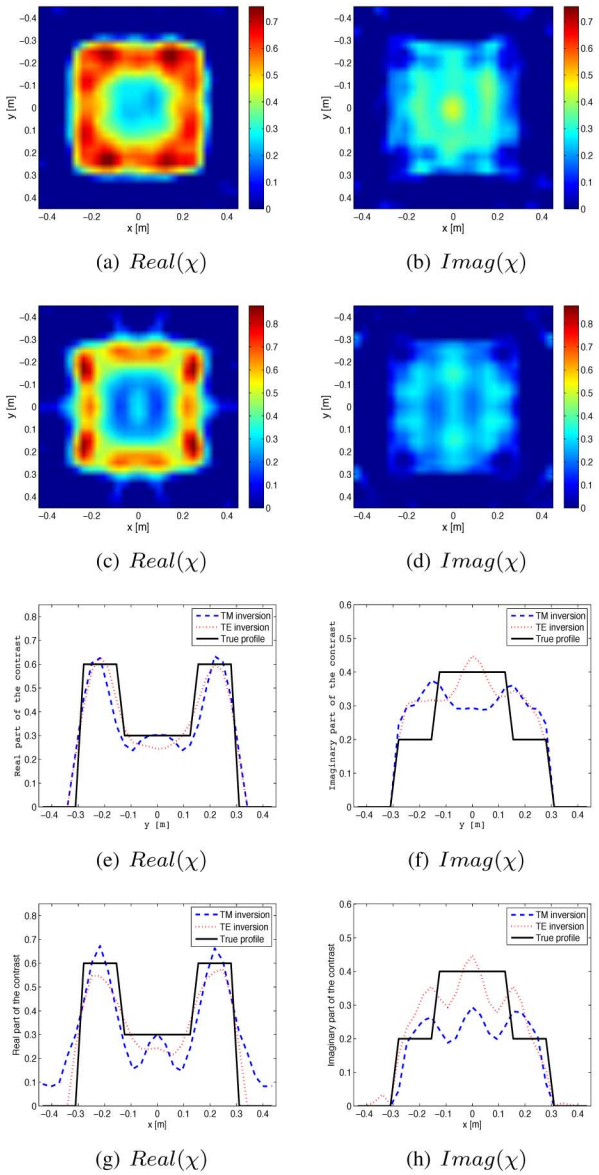

Fig. 13. Inversion of the synthetic data set (the first scenario: $T_x = 10$ and $R = R_x = 10$) using the GNI-CGLS method (a)–(b) TE case (c)–(d) TM case (e)–(f) cross-section at $x = 0$ (g)–(h) cross-section at $y = 0$. (a) $Real(\chi)$. (b) $Imag(\chi)$. (c) $Real(\chi)$. (d) $Imag(\chi)$. (e) $Real(\chi)$. (f) $Imag(\chi)$. (g) $Real(\chi)$. (h) $Imag(\chi)$.

Fig. 11, the TE inversion converged faster than the TM inversion.

To check the sensitivity of the convergence rate to the line search algorithm described in Section III, we have also used another line search technique. This line search algorithm uses the Matlab function *fminsearch* which is based on the simplex method [50]. As opposed to the line search algorithm presented in Section III, this method does not require the derivative of the cost-functional. Applying this line search algorithm at each iteration of the GNI method, the TE inversion required equal or less iterations than the TM inversion to converge. For example, the convergence of the GNI-CGLS method applied to the single-frequency *FoamTwinDiel* case ($f = 6$ GHz) for both TE and TM polarizations using this line search algorithm is shown in Fig. 15

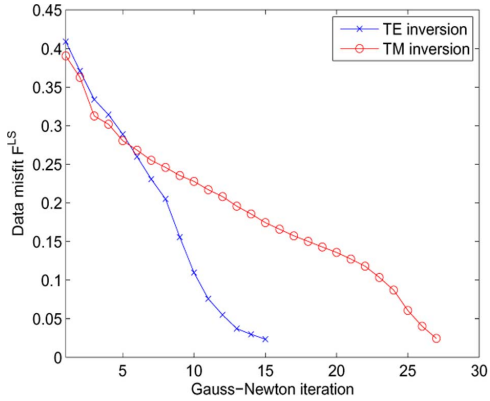

Fig. 14. The data misfit $\mathcal{F}^{\mathcal{LS}}$ for the single-frequency inversion of the *FoamTwinDiel* target at $f = 6\,\mathrm{GHz}$ using the GNI-CGLS method.

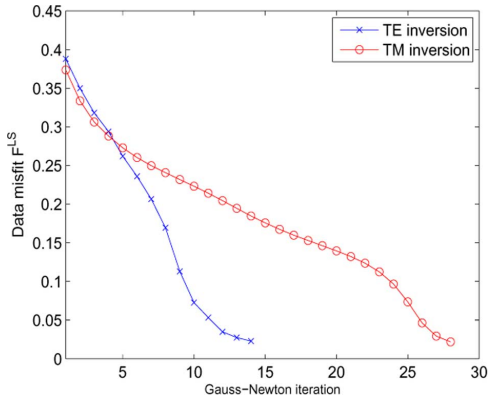

Fig. 15. The data misfit $\mathcal{F}^{\mathcal{LS}}$ for the single-frequency inversion of the *FoamTwinDiel* target at $f = 6$ GHz using the GNI-CGLS method with the derivative-free line search algorithm.

where the TE and TM inversions converged in 14 and 28 iterations respectively. It can easily be seen that this convergence is very similar to the convergence of the GNI-CGLS method using the derivative-based line search algorithm shown in Fig. 14.

VIII. Discussion and Conclusion

We have shown how the recently developed regularized cost functional [5] can be optimized using the Gauss-Newton method in conjunction with a CG-FFT forward solver accelerated by a marching-on-in-source-position technique and applied to the experimental and synthetic data sets in both TE and TM polarizations. For testing this approach, the experimental Fresnel data set was used to provide far-field scattering data and a synthetic data set was used to provide near-field and far-field scattering data. The TE inversions in all cases were compared with the TM inversions in terms of the reconstruction accuracy, convergence rate and theoretical computational complexity.

For all Fresnel targets, the TE and TM inversions are very similar. This is probably due to the fact that the measured data is collected in the far-field where only one scalar field component is required to represent the electric field vector: $E_{\varphi}^{\mathrm{meas}}$ in the TE case and E_{z}^{meas} in the TM case. Thus, in the far-field, splitting $E_{\varphi}^{\mathrm{meas}}$ into E_{x}^{meas} and E_{y}^{meas} does not provide more information than the TM case. In the first scenario of the synthetic test case, where $T_x = 10$ and $R_x = R = 10$ and the collected data

is in the near-field, the TE inversion provides more accurate reconstruction compared to the TM inversion. This is likely due to the fact that E_x^{meas} and E_y^{meas} provide non-redundant information for the TE inversion whereas the TM inversion only utilizes the E_z^{meas} field. However, when the number of transmitters and receivers increases to 30 for the same test case, the TE and TM inversions provide similar results which verifies the fact that the TM inversion lacked enough information compared to the TE case when $T_x = R_x = R = 10$. Keeping the number of transmitters and receivers as in the first scenario but placing them in the far-field (the third scenario), the TE and TM inversions result in a similar reconstruction. This is consistent with the similar performance of TE and TM inversions of Fresnel data set.

In all cases considered in this paper, the TE inversion requires the same or fewer number of iterations than the TM inversion to converge (of course, for the same convergence criteria listed in Section III). The same observation has been reported in [32] where the TE Iterative Multi-Scaling Approach (IMSA) converged faster than the TM IMSA when the signal to noise ratio of the collected data was low. Also, in [51], it has been theoretically speculated that the TE inversion has a lower degree of nonlinearity compared to the TM case which may result in a faster convergence in the TE case. In addition, the actual computational cost of the TE and TM inversions were very close to the approximate theoretical ones presented in Section V.

To verify these results using another regularization technique, we have also inverted these data sets using the CGLS regularization scheme. The conclusion from inversion results obtained from the GNI-CGLS method is consistent with that obtained from the GNI method with the additive-multiplicative regularizer. We have also used another line search algorithm which is a derivative-free method which resulted in a similar convergence compared to the derivative-based line search method.

Considering all this numerical data, we speculate that the ultimate performance and convergence of the GNI algorithm applied to these data sets are highly dependent on the information content of the field, irrespective of the regularization and line search strategies. Thus, the TE inversion, which utilizes both rectangular components of the electric vector at each receiver position, may result in more accurate reconstruction than the TM inversion when utilizing near-field scattering data collected using only a few transmitters and receivers. This paper serves as a preliminary study to compare the performance of the scalar and vectorial inversions and may lead to a theoretical comparison between the performance of these two inversions.

ACKNOWLEDGMENT

The authors would like to thank Institut Fresnel, France, for providing the experimental data set.

REFERENCES

[1] A. Kirsch, *An Introduction to the Mathematical Theory of Inverse Problems*. New York: Springer-Verlag, 1996.

[2] W. C. Chew and Y. M. Wang, "Reconstruction of two-dimensional permittivity distribution using the distorted born iterative method," *IEEE Trans. Med. Imaging*, vol. 9, no. 2, pp. 218–225, 1990.

[3] N. Joachimowicz, C. Pichot, and J. P. Hugonin, "Inverse scattering: An iterative numerical method for electromagnetic imaging," *IEEE Trans. Antennas Propag.*, vol. 39, no. 12, pp. 1742–1752, Dec. 1991.

[4] A. Franchois and A. G. Tijhuis, "A Quasi-Newton reconstruction algorithm for a complex microwave imaging scanner environment," *Radio Sci.*, vol. 38, no. 2, 2003.

[5] J. D. Zaeytijd, A. Franchois, C. Eyraud, and J. Geffrin, "Full-wave three-dimensional microwave imaging with a regularized Gauss-Newton method-theory and experiment," *IEEE Trans. Antennas Propag.*, vol. 55, no. 11, pp. 3279–3292, Nov. 2007.

[6] S. Caorsi, A. Massa, and M. A. Pastorino, "A computational technique based on a real-coded genetic algorithm for microwave imaging purposes," *IEEE Trans. Geosci. Remote Sensing*, vol. 38, pp. 1697–1708, 2000.

[7] T. Rubæk, P. M. Meaney, P. Meincke, and K. D. Paulsen, "Nonlinear microwave imaging for breast-cancer screening using Gauss-Newton's method and the CGLS inversion algorithm," *IEEE Trans. Antennas Propag.*, vol. 55, no. 8, pp. 2320–2331, Aug. 2007.

[8] A. Abubakar, T. M. Habashy, V. L. Druskin, L. Knizhnerman, and D. Alumbaugh, "2.5D forward and inverse modeling for interpreting low-frequency electromagnetic measurements," *Geophysics*, vol. 73, no. 4, pp. F165–F177, Jul.-Aug. 2008.

[9] A. E. Souvorov, A. E. Bulyshev, S. Y. Semenov, R. H. Svenson, A. G. Nazarov, Y. E. Sizov, and G. P. Tastis, "Microwave tomography: A two dimensional newton iterative scheme," *IEEE Trans. Microw. Theory Tech.*, vol. 46, no. 11, pp. 1654–1659, Nov. 1998.

[10] T. M. Habashy and A. Abubakar, "A general framework for constraint minimization for the inversion of electromagnetic measurements," *Progr. Electromagn. Res.*, vol. 46, pp. 265–312, 2004.

[11] A. Franchois and C. Pichot, "Microwave imaging-complex permittivity reconstruction with a Levenberg-Marquardt method," *IEEE Trans. Antennas Propag.*, vol. 45, no. 2, pp. 203–215, Feb. 1997.

[12] C. Gilmore, P. Mojabi, and J. LoVetri, "Comparison of an enhanced distorted born iterative method and the multiplicative-regularized contrast source inversion method," *IEEE Trans. Antennas Propag.*, vol. 57, no. 8, pp. 2341–2351, Aug. 2009.

[13] P. Mojabi and J. LoVetri, "Microwave biomedical imaging using the multiplicative regularized Gauss-Newton inversion," *IEEE Antennas Wireless Propag. Lett.*, vol. 8, pp. 645–648, 2009.

[14] R. E. Kleinman and P. M. van den Berg, "A modified gradient method for two-dimensional problem in tomography," *J. Comput. Appl. Math.*, vol. 42, no. 1, pp. 17–35, 1992.

[15] P. M. van den Berg and R. E. Kleinman, "A contrast source inversion method," *Inverse Probl.*, vol. 13, pp. 1607–1620, 1997.

[16] A. Abubakar and P. M. van den Berg, "Iterative forward and inverse algorithms based on domain integral equations for three-dimensional electric and magnetic objects," *J. Comput. Phys.*, vol. 195, pp. 236–262, 2004.

[17] A. E. Bulyshev, A. E. Souvorov, S. Y. Semenov, V. G. Posukh, and Y. E. Sizov, "Three dimensional vector microwave tomography: Theory and computational experiments," *Inverse Probl.*, vol. 20, pp. 1239–1259, 2004.

[18] A. Litman and L. Crocco, "Testing inversion algorithms against experimental data: 3D targets," *Inverse Probl.*, vol. 25, 2009.

[19] P. Meaney, K. Paulsen, S. Geimer, S. Haider, and M. Fanning, "Quantification of 3-D field effects during 2-D microwave imaging," *IEEE Trans. Biomed. Eng.*, vol. 49, pp. 708–720, Jul. 2002.

[20] B. J. Kooij and P. M. van den Berg, "Nonlinear inversion in TE scattering," *IEEE Trans. Microw. Theory Tech.*, vol. 46, pp. 1704–1712, Nov. 1998.

[21] G. P. Otto and W. C. Chew, "Inverse scattering of H_z waves using local-shape function imaging: a T-matrix formulation," *Int. J. Imag. Syst. Technol.*, vol. 5, pp. 22–27, 1994.

[22] A. Abubakar and T. M. Habashy, "Nonlinear inversion of multi-frequency microwave Fresnel data using the multiplicative regularized contrast source inversion," *Progr. Electromagn. Res.*, vol. 62, pp. 193–201, 2006.

[23] C. P. Cho and Y. W. Kiang, "Inverse scattering of dielectric cylinders by a cascaded TE-TM method," *IEEE Trans. Microw. Theory Tech.*, vol. 47, no. 10, pp. 1923–1930, Oct. 1999.

[24] C. Pichot, J. Y. Dauvignac, I. Aliferis, E. L. Brusq, R. Ferrayé, and V. Chatelée, "Recent nonlinear inversion methods and measurement system for microwave imaging," presented at the IEEE Int. Workshop on Imaging Systems and Techniques, Stresa, Italy, May 2004.

[25] K. Belkebir and M. Saillard, "Special section: Testing inversion algorithm against experimental data," *Inverse Probl.*, vol. 17, pp. 1565–1571, 2001.

[26] C. Ramananjoana, M. Lambert, and D. Lesselier, "Shape inversion from TM and TE real data by controlled evolution of level sets," *Inverse Probl.*, vol. 17, pp. 1585–1595, 2001.

[27] R. F. Bloemenkamp, A. Abubakar, and P. M. van den Berg, "Inversion of experimental multi-frequency data using the contrast source inversion method," *Inverse Probl.*, vol. 17, pp. 1611–1622, 2001.
[28] J.-M. Geffrin, P. Sabouroux, and C. Eyraud, "Free space experimental scattering database continuation: experimental set-up and measurement precision," *Inverse Probl.*, vol. 21, pp. S117–S130, 2005.
[29] K. Belkebir and M. Saillard, "Testing inversion algorithms against experimental data: inhomogeneous targets," *Inverse Probl.*, vol. 21, pp. S1–S3, 2005.
[30] A. Abubakar, P. M. van den Berg, and T. M. Habashy, "Application of the multiplicative regularized contrast source inversion method on TM- and TE-polarized experimental fresnel data," *Inverse Probl.*, vol. 21, pp. S5–S13, 2005.
[31] C. Yu, L. P. Song, and Q. H. Liu, "Inversion of multi-frequency experimental data for imaging complex objects by a DTA-CSI method," *Inverse Probl.*, vol. 21, pp. S167–S178, 2005.
[32] D. Franceschini, M. Donell, G. Franceschini, and A. Massa, "Iterative image reconstruction of two-dimensional scatterers illuminated by TE waves," *IEEE Trans. Microw. Theory Tech.*, vol. 54, no. 4, pp. 1484–1494, Apr. 2006.
[33] O. Féron, B. Duchêne, and A. Mohammad-Djafari, "Microwave imaging of piecewise constant objects in a 2D-TE configuration," *Int. J. Appl. Electromagn. Mechan.*, vol. 26, pp. 167–174, 2007.
[34] K. Paulsen and P. Meaney, "Nonactive antenna compensation for fixed-array microwave imaging—I. model development," *IEEE Trans. Med. Imag.*, vol. 18, pp. 496–507, Jun. 1999.
[35] J. Ma, W. C. Chew, C. C. Lu, and J. Song, "Image reconstruction from TE scattering data using equation of strong permittivity fluctuation," *IEEE Trans. Antennas Propag.*, vol. 48, no. 6, pp. 860–867, Jun. 2000.
[36] E. Chong and S. Zak, *An Introduction to Optimization*. New York: Wiley Interscience, 2001.
[37] J. D. Zaeytijd and A. Franchois, "Three-dimensional quantitative microwave imaging from measured data with multiplicative smoothing and value picking regularization," *Inverse Probl.*, vol. 25, 2009.
[38] P. Mojabi and J. LoVetri, "Overview and classification of some regularization techniques for the Gauss-Newton inversion method applied to inverse scattering problems," *IEEE Trans. Antennas Propag.*, vol. 57, no. 9, pp. 2658–2665, Sep. 2009.
[39] M. S. Zhdanov, *Geophysical Inverse Theory and Regularization*. Amsterdam: Elsevier, 2002.
[40] A. G. Tijhuis, K. Belkebir, and A. C. S. Litman, "Theoretical and computational aspects of 2-D inverse profiling," *IEEE Trans. Geosci. Remote Sensing*, vol. 39, pp. 1316–1330, 2001.
[41] P. R. McGillivray and D. W. Oldenburg, "Methods for calculating Fréchet derivatives and sensitivities for the non-linear inverse problem," *Geophys. Prospect.*, vol. 38, pp. 499–524, 1990.
[42] T. K. Jensen, "Stabilization Algorithms for Large-Scale Problems," Ph.D. dissertation, Technical Univ. Denmark, Kongens Lyngby, Denmark, 2006.
[43] P. C. Hansen, "Deconvolution and regularization with Toeplitz matrices," *Numer. Algorithms*, vol. 29, pp. 323–378, 2002.
[44] A. Abubakar, P. M. van den Berg, and S. Y. Semenov, "A robust iterative method for born inversion," *IEEE Trans. Geosci. Remote Sensing*, vol. 42, pp. 342–354, Feb. 2004.
[45] P. M. van den Berg, A. L. van Broekhoven, and A. Abubakar, "Extended contrast source inversion," *Inverse Probl.*, vol. 15, pp. 1325–1344, 1999.
[46] W. C. Chew and J. H. Lin, "A frequency-hopping approach for microwave imaging of large inhomogeneous bodies," *IEEE Microw. Guided Wave Lett.*, vol. 5, pp. 439–441, Dec. 1995.
[47] P. Mojabi and J. LoVetri, "Enhancement of the Krylov subspace regularization for microwave biomedical imaging," *IEEE Trans. Med. Imag.*, vol. 28, no. 12, pp. 2015–2019, Dec 2009.
[48] P. C. Hansen, *Rank-Deficient and Discrete Ill-Posed Problems: Numerical Aspects of Linear Inversion*. Philadelphia, PA: SIAM Review, 1998.
[49] P. C. Hansen, "Analysis of discrete ill-posed problems by means of the L-curve," *SIAM Review*, vol. 34, no. 4, pp. 561–580, Dec. 1992.
[50] J. Lagarias, J. A. Reeds, M. H. Wright, and P. E. Wright, "Convergence properties of the Nelder-Mead simplex method in low dimensions," *SIAM J. Optimization*, vol. 9, no. 1, pp. 112–147, 1998.
[51] O. M. Bucci, N. Cardace, L. Crocco, and T. Isernia, "2D inverse scattering: degree of nonlinearity, solution strategies and polarization effects," *Proc. SPIE*, vol. 4123, pp. 185–193, 2000.

Puyan Mojabi (S'09) received the B.Sc. degree in electrical and computer engineering from the University of Tehran, Tehran, Iran, in 2002 and the M.Sc. degree in electrical engineering from Iran University of Science and Technology, Tehran, in 2004. Currently, he is working toward the Ph.D. degree at the University of Manitoba, Winnipeg, MB, Canada.

His current research interests are computational electromagnetics and inverse problems.

Joe LoVetri (SM'09) was born in Enna, Italy, in 1963. He received the B.Sc. (with distinction) and M.Sc. degrees, both in electrical engineering, from the University of Manitoba, Winnipeg, MB, Canada, in 1984 and 1987, respectively, and the Ph.D. degree in electrical engineering from the University of Ottawa, Ottawa, ON, Canada, in 1991.

From 1984 to 1986, he was an EMI/EMC Engineer at Sperry Defence Division, Winnipeg, Manitoba. From 1986 to 1988, he held the position of TEMPEST Engineer at the Communications Security Establishment, Ottawa. From 1988 to 1991, he was a Research Officer at the Institute for Information Technology, National Research Council of Canada. From 1991 to 1999, he was an Associate Professor in the Department of Electrical and Computer Engineering, the University of Western Ontario. In 1997/98, he spent a sabbatical year at the TNO Physics and Electronics Laboratory, The Netherlands. Since 1999, he has been a Professor in the Department of Electrical and Computer Engineering, University of Manitoba, and was Associate Dean, Research, from 2004 to 2009. His main interests lie in time-domain computational electromagnetics, modeling of electromagnetic compatibility problems, microwave tomography and inverse problems.